

Multifrequency study of a double–double radio galaxy J0028+0035

A. Marecki^{1*}, M. Jamrozy², J. Machalski², U. Pajdosz-Śmierciak²

¹*Institute of Astronomy, Nicolaus Copernicus University, Faculty of Physics, Astronomy and Informatics, ul. Grudziądzka 5, PL-87-100 Toruń, Poland*

²*Astronomical Observatory, Jagiellonian University, ul. Orla 171, PL-30-244 Kraków, Poland*

Accepted 2020 November 16. Received 2020 November 16; in original form 2020 July 31

ABSTRACT

We report the discovery of a double–double radio source (DDRS) J0028+0035. We observed it with LOFAR, GMRT, and the VLA. By combining our observational data with those from the literature, we gathered an appreciable set of radio flux density measurements covering the range from 74 MHz to 14 GHz. This enabled us to carry out an extensive review of physical properties of the source and its dynamical evolution analysis. In particular, we found that, while the age of the large-scale outer lobes is about 245 Myr, the renewal of the jet activity, which is directly responsible for the double–double structure, took place only about 3.6 Myr ago after about 11 Myr long period of quiescence. Another important property typical for DDRSs and also present here is that the injection spectral indices for the inner and the outer pair of lobes are similar. The jet powers in J0028+0035 are similar too. Both these circumstances support our inference that it is, in fact, a DDRS which was not recognized as such so far because of the presence of a coincident compact object close to the inner double so that the centre of J0028+0035 is apparently a triple.

Key words: radiation mechanisms: non-thermal — galaxies: active — galaxies: individual: J0028+0035 — galaxies: jets — radio continuum: galaxies

1 INTRODUCTION

Intermittent nature of the activity is a well-known property of active galactic nuclei (AGN). The most compelling observable signature of cessation and subsequent restart of activity in a radio-loud AGN takes the form of a double–double radio source (DDRS) that consists of two co-linear pairs of radio lobes (Schoenmakers et al. 2000a). The outer lobes develop during the earlier active period. Once the active nucleus becomes quiescent, the supply of relativistic particles via jets to the lobes is cut off, and they gradually fade out. Quiescence can last for up to 10^8 yr (Komissarov & Gubanov 1994). Nevertheless, having not been fuelled even for such a long time, the lobes may still be visible; they usually appear as diffuse relics. Meanwhile, the renewal of activity of the nucleus may occur, which leads to the creation of a new pair of lobes – the inner one. The possibility that they emerge *before* the outer lobes disappear is the reason why the overall radio structure is double–double.

Nearly a hundred of DDRSs are known to date (see e.g. Saikia & Jamrozy 2009; Nandi & Saikia 2012; Kuźmicz et al. 2017; Mahatma et al. 2019). Some of them have unusual properties. There are three objects with clear evidence of possessing even three pairs of lobes, so they are labelled triple-double radio sources. These are: J0929+4146 (Schoenmakers et al. 2000a; Brocksopp et al. 2007), J1409–0302 (Specia; Hota et al. 2011), and J1216+0709 (Singh et al. 2016). Two DDRSs, J0935+0204

(4C 02.27; Jamrozy, Saikia & Konar 2009) and J0741+3112 (Siemiginowska et al. 2003), are hosted by quasars, whereas J2345–0449 (Bagchi et al. 2014) and again J1409–0302 – both of giant sizes – are hosted by spiral galaxies. Another exceptional case of restarting activity is the giant radio galaxy J2333–2343 (Hernandez-Garcia et al. 2017) where the direction of the jet has changed in the new episode of nuclear activity; it points almost towards us now which makes this source a radio galaxy with a blazar host. J1647+4950 (SBS B1646+499; Pajdosz-Śmierciak et al. 2018) with large-scale diffuse lobes is also hosted by a blazar.

Surprisingly, a relatively small number of DDRSs were thoroughly studied. These are: 1548–3216 (Machalski, Jamrozy & Konar 2010), J1453+3308 (Konar et al. 2006), J0041+3224 and J1835+6204 (Konar et al. 2012, 2013), J1352+3126 (Machalski et al. 2016), and J1706+4340 for which Marecki, Jamrozy & Machalski (2016) determined a range of astrophysical parameters such as dynamical and synchrotron ages, and the ambient medium characteristics. In particular, they found that the large-scale outer lobes of J1706+4340 are up to 300 Myr old whereas the renewal of the jet activity took place only about 12 Myr ago after about 27-Myr long period of quiescence. This result is yet another but very compelling proof that the explanation of the nature of DDRSs proposed by Schoenmakers et al. (2000a) is correct. The correctness of their model can also be demonstrated when studying a sample of DDRSs selected from a large survey like *Faint Images of the Radio Sky at Twenty centimetres* (FIRST;

* E-mail: amr@astro.uni.torun.pl

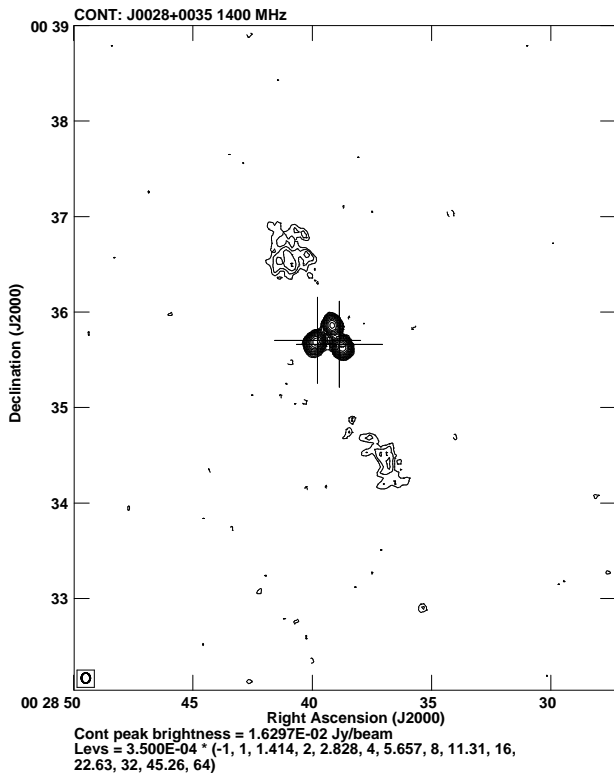


Figure 1. FIRST image of J0028+0035. The optical position of the BL Lac object 5BZU J0028+0035 is marked with the left-hand cross. The position of SDSS J002838.86+003539.7 galaxy is marked with the right-hand cross.

Becker et al. 1995). This has been carried out in three steps. The initial selection was made by Proctor (2011) who found 242 DDRS candidates. Secondly, 23 of them were verified as true DDRSs by Nandi & Saikia (2012). Finally, the sample was surveyed with the Giant Metrewave Radio Telescope (GMRT, Swarup et al. 1991) by Nandi et al. (2019). Using both 607-MHz and the FIRST images, they estimated spectral indices of the inner and the outer lobes of each source. For the vast majority of them, the spectra of their outer lobes were significantly steeper in line with Schoenmakers et al. (2000a).

When searching FIRST for the large-scale structures centred on the objects from Roma-BZCAT, a multifrequency catalogue of blazars (Massaro et al. 2009), we discovered that the BL Lac object 5BZU J0028+0035, also known as SDSS J002839.77+003542.2, not only was straddled by large-scale relic lobes but also accompanied by two other compact components located close enough to it (in terms of the angular distance) to be straddled by those relics as well. We suggest that the only way to interpret the triple structure at the centre of J0028+0035 – see Fig. 1 – is to assume that 5BZU J0028+0035 is a coincidence. It follows that since the relic lobes and the inner two components at RA = 00^h28^m38^s.76, Dec. = +00°35′38″.1 and RA = 00^h28^m39^s.16, Dec. = +00°35′51″.6 are co-linear, J0028+0035 could be a DDRS. In other words, it appears that this is because of the presence of 5BZU J0028+0035 that J0028+0035 was not recognized as a DDRS so far. To support the classification of J0028+0035 as a DDRS, its optical identification and higher resolution observations of its putative inner lobes are needed. Obviously, the host galaxy must lie between them. SDSS J002838.86+003539.7 is the only candidate here; it is marked with the right-hand cross in Fig. 1. As for the radio mor-

phology of the alleged inner lobes, revealing it is desirable because they are unresolved in the FIRST image (Fig. 1). Therefore, based on that image alone, it is not possible either to rule out the possibility that the inner triple is a result of e.g. gravitational lensing or to confirm whether the morphologies of the two western components are typical for the lobes. Owing to the observations we have carried out, we are able to address this issue. Furthermore, we analyse all available radio data on J0028+0035 in order to study its dynamics and energetics.

The paper is organized as follows. Multifrequency radio data are presented in Section 2. The dynamical analysis of each pair of radio lobes of J0028+0035 is elaborated upon in Section 3. The results are discussed in Section 4 and summarized in Section 5. For consistency with the analyses conducted in our earlier papers, the cosmological parameters by Spergel et al. (2003, $H_0 = 71 \text{ km s}^{-1} \text{ Mpc}^{-1}$, $\Omega_M = 0.27$, $\Omega_\Lambda = 0.73$) are used throughout this article. Positions are given in the J2000.0 coordinate system.

2 RADIO DATA ON J0028+0035

Here, we present high-resolution images of the putative inner lobes and new images of the overall radio structure of J0028+0035 resulting from our observations with LOw-Frequency ARray (LOFAR, van Haarlem et al. 2013), GMRT, and the Karl G. Jansky Very Large Array (VLA). Based on that material and the literature, we have collected radio flux densities in the range from 74 MHz to 14 GHz for all components of J0028+0035. Our data base is characterized in Table 1.

2.1 LOFAR observations

Dedicated observations of J0028+0035 with LOFAR (project code: LC8_007) were conducted in August 2017 (for details see Table 1) in cooperation with the LOFAR Two-metre Sky Survey (LoTSS) Tier-1 Team – see Shimwell et al. (2017) for the survey description. We observed the target in the HBA low-band Dual Inner mode using 24 core and 14 remote LOFAR stations. Total integration time was 8 h, including 10% overhead, with one-second integration time, 244 subbands with 16 channels per subband in 110–190 MHz filter with 200-MHz clock speed. To mitigate the influence of the ionosphere, we required the target’s elevation to be over 30° above the horizon during the observations. Source 3C 48 was used as a flux density and bandpass calibrator in 10-min runs at the beginning and the end of the observations.

Standard reduction as well as flux density, phase, and bandpass calibration were provided by the Radio Observatory and the Tier-1 Survey Team. Due to low observing frequency, large field of view of the instrument ($\sim 5^\circ$), and low declination of the target, we decided to increase the accuracy of the final map through the Prefactor pipeline,¹ which prepares the data to any direction-dependent calibration and includes i.a. advanced flagging and removal of the initial clock offsets between the core and remote stations. Then, we applied the direction-dependent LOFAR Facet Calibration described in van Weeren et al. (2016). Both pipelines were run on CEP3 cluster allocated by the LOFAR Program Committee and the International LOFAR Telescope (ILT) director during the regular proposal evaluation stage. Apart from that, direction-dependent calibration and imaging were provided by the Tier-1 Survey Team

¹ <https://github.com/lofar-astron/prefactor/>

Table 1. Radio data of J0028+0035 analysed in this study

Frequency (MHz)	Telescope/Survey	Date of observation	Beam size (arcsec)		Beam PA (°)	rms (mJy beam ⁻¹)	Reference
(1)	(2)	(3)	(4)		(5)	(6)	(7)
73.8	VLA-B/VLSSr	2003 Sep. 20	75	75	0	180.7	1
76–227	MWA/GLEAM	2013 Nov. 15	324.2 – 118.0	295.7 – 106.6		95 – 20	2
143.7	LOFAR HBA	2017 Aug. 18	14.54	6.25	76.1	1.0	p
147.6	LOFAR HBA	2017 Aug. 18	12	12	0	1.7	p
322.7	GMRT	2017 Sep. 14	9.43	7.79	74.73	0.09978	p
607.7	GMRT	2017 Sep. 10	5.34	4.14	61.39	0.1135	p
607.7 ^a	GMRT	2017 Sep. 10	12.49	7.95	-36.36	0.2375	p
1400.0	VLA-D/NVSS	1993 Nov. 15	45	45	0	0.45	3
1400.0	VLA-B/FIRST	1995 Sep. 23	6.40	5.4	0	0.11	4
1437.4	GMRT	2017 Sep. 5	4.37	3.60	82.09	0.0788	p
1519.4	VLA-A	2018 Apr. 18	2.47	1.01	-50.95	0.0895	p
3000.0	VLA-B/VLASS	2017 Sep. 29	2.76	2.16	-7.52	0.1033	5
4850.0	Green Bank 91m/87GB	1986-1987	222	194	0	5	6
5469.1	VLA-C	2018 Nov. 21	7.78	3.02	-51.77	0.0130	p
5494.0	VLA-A	2018 Apr. 2	0.75	0.30	-53.44	0.0138	p
9016.8	VLA-D	2018 Sep. 12	15.87	7.21	49.36	0.0160	p
14014.9	VLA-D	2018 Sep. 12	9.68	4.38	49.12	0.016	p

References – (1) Lane et al. (2014); (2) Hurley-Walker et al. (2017); (3) Condon et al. (1998); (4) Becker et al. (1995); (5) Lacy et al. (2020); (6) Gregory & Condon (1991); (p) this paper. ^aData in this line has been extracted from the tapered map.

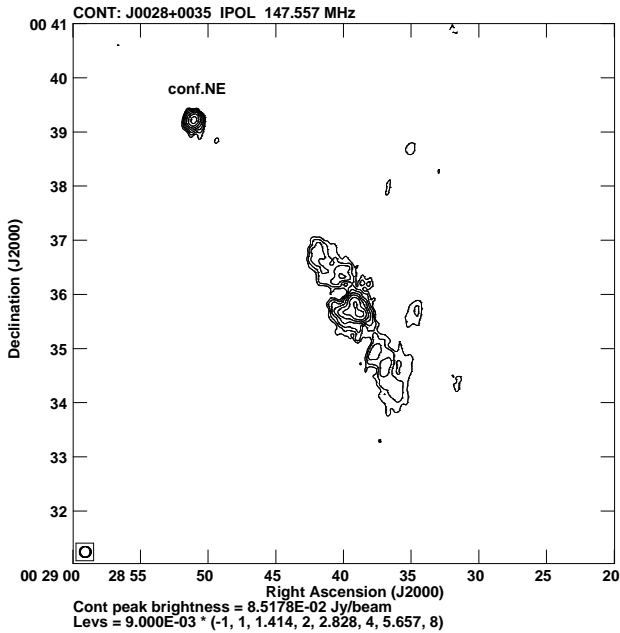


Figure 2. LOFAR HBA image of J0028+0035 encompassing coincident conf. NE source.

with the use of ddf-pipeline.² We were able to resolve the central region of J0028+0035 using Facet Calibration method whereas the extended, diffuse lobes were better calibrated and imaged with ddf-pipeline. The latter also allowed for better handling of interference from strong (above 1.3 Jy at 147.6 MHz) northern source

² <https://github.com/mhardcastle/ddf-pipeline/>

4C+00.03. The resolutions of the maps attained after application of Facet Calibration and ddf-pipeline were 14.54×6.25 arcsec² and 12×12 arcsec², respectively, with the corresponding rms noise levels of 1 and 1.7 mJy beam⁻¹.

The LOFAR image of the total structure of J0028+0035 is shown in Fig. 2 that also features a relatively strong coincident source towards north-east from the target source, afterwards referred to as conf. NE. The reference to the figure where the central structure of J0028+0035 observed with LOFAR is shown is given at the end of Section 2.3. The flux density measurements for different components of the target source and the conf. NE are shown in Table 2.

2.2 GMRT observations

We performed dedicated observations of J0028+0035 with GMRT in three frequency bands centred at: 323, 608, and 1437 MHz. The project code was 32_008. The observations were conducted in September 2017 (for details see Table 1). Data were recorded with 8-s integration time with the frequency band of 33.3 MHz divided into 512 channels at 323 and 608 MHz or 256 channels at 1437 MHz. The usual scheme of observing phase calibrator interlaced with the observation of the target source was adopted. Phase calibrator J0022+0014 (4C 00.02) was used at each of the observed frequencies. Flux density calibrator 3C 48 was observed for about 15 min at the beginning and at the end of observing at each frequency. The total integration time on the target source, which consisted of several 30-min exposures, was about 6.5, 2.5, and 5.5 h at 323, 608, and 1437 MHz, respectively.

The 323 and 608 MHz data reduction was carried out following standard calibration and reduction procedures in ASTRO-

Table 2. Observed flux densities of different components of J0028+0035

Frequency (MHz)	Total structure	Flux density (mJy)					Outer structure		Reference
		Conf. NE	Central structure			SW lobe	NE lobe		
(1)	(2)	(3)	SW lobe (4)	NE lobe (5)	Core (6)	Blazar (7)	(8)	(9)	(10)
73.8	1593.0 ± 288.0 ^a								1
76	1581.6 ± 158.2	301 ± 97.0							2
84	1463.6 ± 146.4	212 ± 76.5							2
91.5	1297.6 ± 129.8	144 ± 66.7							2
99	1110.0 ± 111.0								2
107	1158.8 ± 115.9								2
114.5	992.5 ± 99.3	203 ± 47.7							2
122	970.4 ± 97.0								2
130	815.7 ± 81.6								2
143	811.3 ± 81.1								2
143.7						81 ± 8	218 ± 33	250 ± 38	p
147.6	824 ± 124		119 ^c ± 12	102 ± 11					p
150.5	793.8 ± 79.4	142 ± 31.4							2
158	750.0 ± 75.0								2
166	732.3 ± 73.2								2
173.5	706.6 ± 70.7	149 ± 32.5							2
181	620.8 ± 62.1								2
189	579.5 ± 58.0								2
196.5	613.8 ± 61.4								2
200.5	585.5 ± 58.6	130 ± 26.4							2
204	568.6 ± 56.9								2
212	540.1 ± 54.0								2
219.5	553.5 ± 55.4	99 ± 23.7							2
227	512.9 ± 51.3								2
322.7	394.2 ± 39.4	71.3 ± 0.8	59.2 ^c ± 6.4	48.9 ± 4.9		51.3 ± 5.1	91.9 ± 9.2	101.0 ± 10.1	p
607.7		30.1 ± 3.0	38.0 ^c ± 4.0	27.5 ± 3.0		30.1 ± 3.3			p
607.7 ^b	218.5 ± 22.0		37.5 ^c ± 3.8	25.9 ± 2.6		35.4 ± 3.6	47.5 ± 4.9	57.4 ± 5.9	p
1400.0	123.9 ± 12.5	11.7 ± 1.5							3
1400.0		10.9 ± 1.0	22.0 ^c ± 2.2	16.5 ± 1.7		20.3 ± 2.0	25.7 ± 2.7 ^d	27.0 ± 2.8 ^d	4
1437.4			22.8 ^c ± 2.3	18.4 ± 1.8		22.5 ± 2.3	28.5 ± 3.0	24.3 ± 2.5	p
1519.4			22.9 ^c ± 2.3	17.9 ± 1.8	8.4 ± 0.9	21.3 ± 2.2			p
3000.0			13.6 ^c ± 1.4	10.1 ± 1.1	4.9 ± 0.5	15.5 ± 1.6			5
4850.0	38 ± 10								6
5469.0			8.5 ^c ± 0.9	6.7 ± 0.7		11.0 ± 1.1	4.9 ± 0.5	5.1 ± 0.5	p
5494.0			7.4 ^c ± 0.8	5.1 ± 0.5	2.7 ± 0.3	9.8 ± 1.0			p
9016.8			5.8 ^c ± 0.6	4.6 ± 0.5		8.5 ± 0.9	2.1 ± 0.2	2.3 ± 0.2	p
14014.9			3.7 ^c ± 0.4	3.3 ± 0.3		6.1 ± 0.6			p

References – (1) Lane et al. (2014); (2) Hurley-Walker et al. (2017); (3) Condon et al. (1998); (4) Becker et al. (1995); (5) Lacy et al. (2020); (6) Gregory & Condon (1991); (p) this paper. ^aThe original flux density of the VLSSr survey (RBC scale; Roger et al. 1973) was multiplied by a factor of 0.9 to suit the Baars et al. (1977) scale. ^bThis has been taken from the tapered map. ^cThis measurement includes also the core flux density. ^dThis measurement is from the combined (with IMERG) FIRST and NVSS map.

NOMICAL IMAGE PROCESSING SYSTEM (AIPS).³ The data processing was automated with a pipeline based on the Source Peeling and Atmospheric Modeling (SPAM) package (Intema 2009, 2014; Intema et al. 2009) that includes direction-dependent calibration, modelling, and corrections for dispersive phase delay which is mainly of ionospheric origin. Data were edited for strong radio frequency interference and then standard flux density, phase, and bandpass calibrations were applied to the source. To produce deconvolved images, we used AIPS IMAGR task in which we subdivided the field of view covering the primary beam into a number of facets. To obtain an image that presents the diffuse outer lobes at

608 MHz properly, we tapered the data at $20 k\lambda$ so that the restoring beam is 12.49×7.95 arcsec². Several rounds of phase-based self-calibration were performed. The resultant image was then corrected for the primary beam using AIPS PBCOR task.

The 1437-MHz data were automatically flagged, reduced, and calibrated with package CASA (COMMON ASTRONOMY SOFTWARE APPLICATIONS),⁴ using a pipeline originally developed by Russ Taylor in 2011 and modified by Ishwara-Chandra et al. (2020). The resulting image was obtained using CASA task tclean and its quality was improved using self-calibration. We tapered the original uv-data to extract the diffuse lobes with the restoring beam of

³ <https://aips.nrao.edu/>⁴ <https://casa.nrao.edu/>

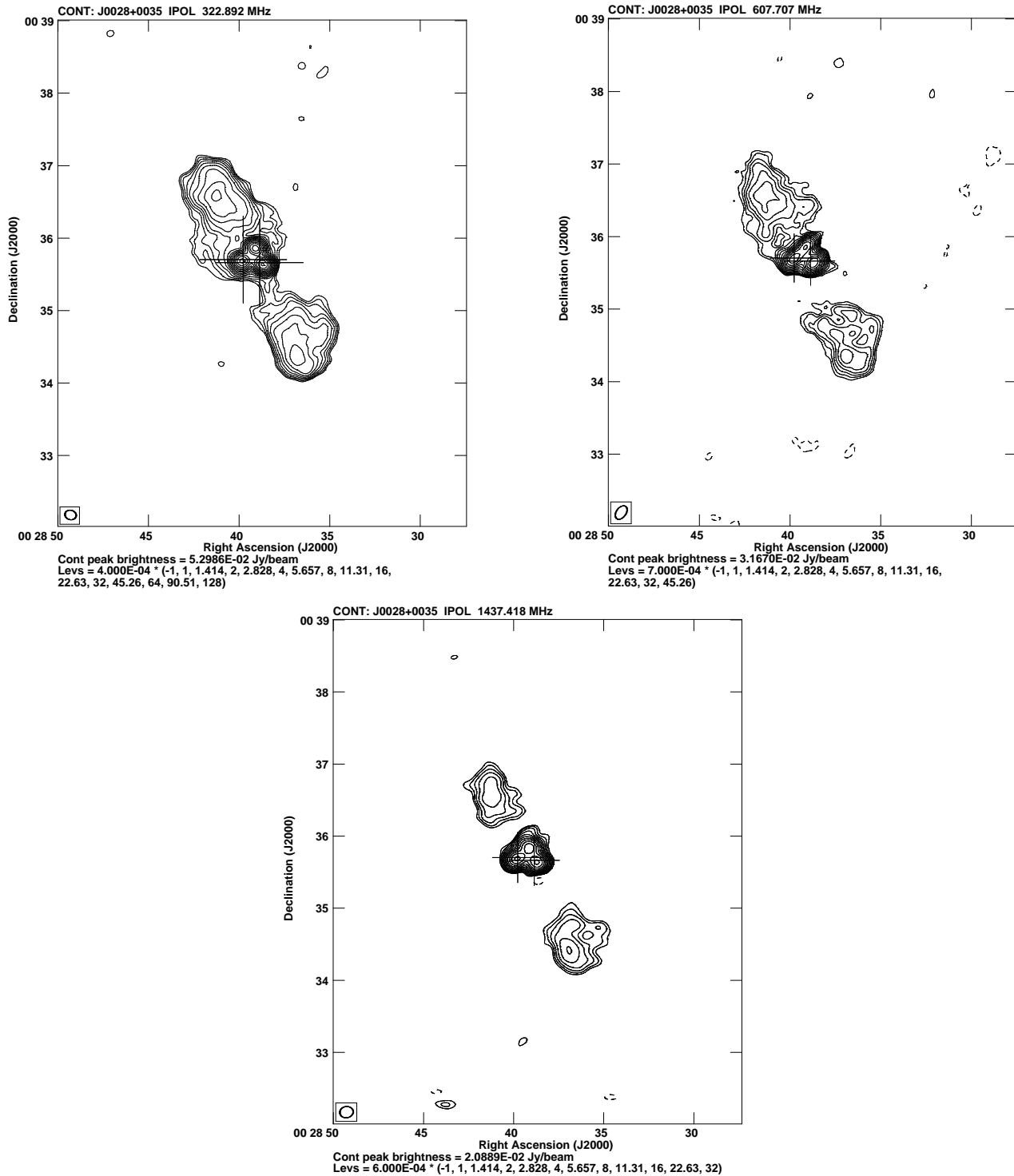


Figure 3. Images of J0028+0035 resulting from the GMRT observations at 323 MHz (upper left-hand panel), 608 MHz (upper right-hand panel), and 1437 MHz (bottom panel). The optical position of the BL Lac object 5BZU J0028+0035 is marked with the left-hand cross. The position of the SDSS J002838.86+003539.7 galaxy is marked with the right-hand cross.

11.17×9.35 arcsec². The image was also corrected for the primary beam.

The GMRT images are shown in Fig. 3⁵. Owing to tapering of 608 and 1437 MHz ones, their resolution is comparable to that

⁵ For consistency, all its panels were plotted with AIPS utility regardless of whether the images were generated in AIPS or in CASA.

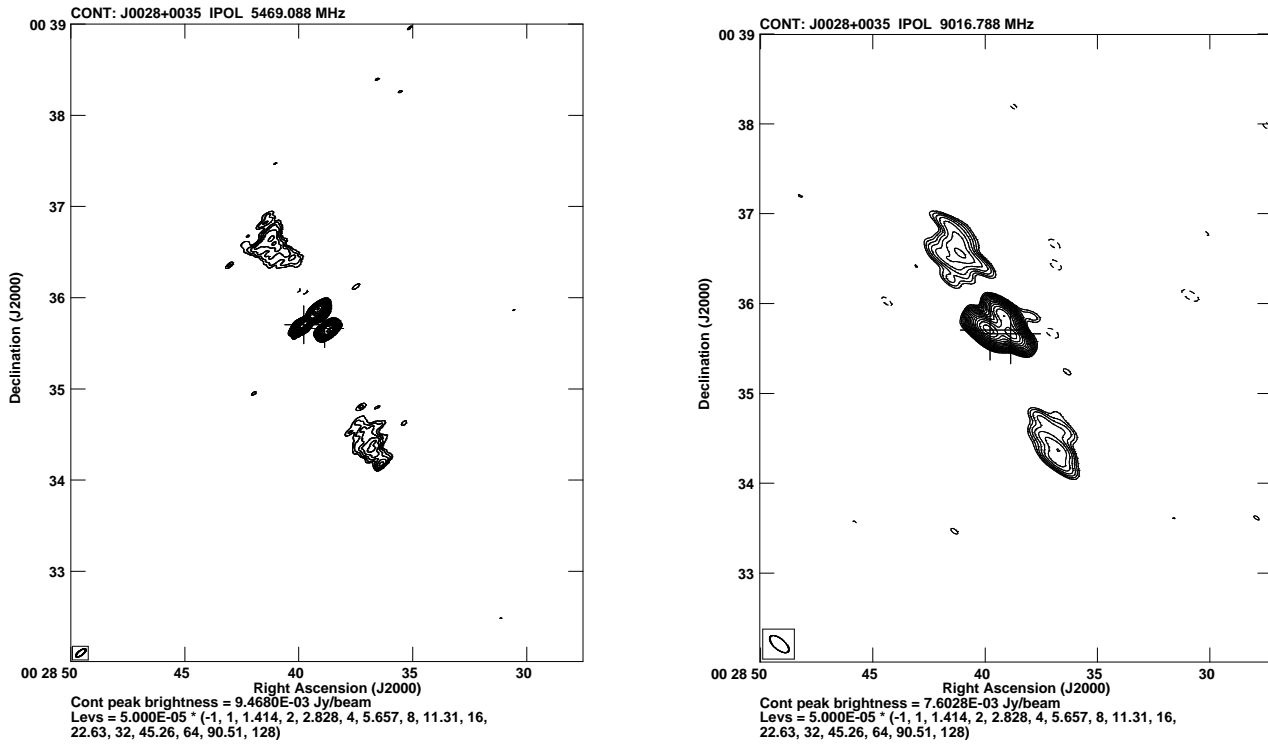


Figure 4. The VLA observations at 5469 MHz in C conf. (left-hand panel) and at 9017 MHz in D conf. (right-hand panel). The optical position of the BL Lac object 5BZU J0028+0035 is marked with the left-hand cross. The position of the SDSS J002838.86+003539.7 galaxy is marked with the right-hand cross.

of the 323-MHz image (9.43×7.79 arcsec²). The flux density measurements and their errors are shown in Table 2. The flux density calibration errors are assumed to be 10% at all three frequencies.

2.3 VLA observations

Five dedicated observations of J0028+0035 with the VLA in three configurations at four frequencies were conducted. They are listed in Table 1 in the lines denoted with ‘VLA-A’, ‘VLA-C’, and ‘VLA-D’ in column 2. Standard continuum processing with VLA CASA Calibration Pipeline was carried out. Final images were obtained with AIPS task IMAGR. Fig. 4 presents the overall structure of J0028+0035 at 5469 and 9017 MHz but with unresolved inner lobes whereas in Fig. 5, the inner lobes are shown in full detail while the outer lobes are not present either due to the ‘missing flux’ effect caused by the resolution in A conf. (lower panels) or due to steepness of the spectrum of the outer lobes so that they are not visible at 14 GHz (upper right-hand panel). The LOFAR image of the inner triple has been included as the fourth, upper left-hand panel of Fig. 5. The flux density measurements for different components of the target source and the errors of those measurements are shown in Table 2.

2.4 Data extracted from surveys

In Table 2, we also display a number of data from the literature. The lowest frequency at which we have data for our target is 74 MHz. We used the *VLA Low-Frequency Sky Survey* redux (VLSSr; Lane et al. 2012, 2014) that covers the sky north of declination -30° . The VLSSr represents a major improvement

(e.g. correction of the ionospheric distortions and increase of dynamic range, as well as revision of the primary beam correction) to the original VLSS (Cohen et al. 2007). The VLSSr has a resolution of 75×75 arcsec² and an average map rms noise level of ~ 0.1 Jy beam⁻¹. The VLSSr maps and catalogue use the Roger et al. (1973) flux density scale.

The second public survey we used was the *GaLactic and Extragalactic All-sky MWA* (GLEAM) survey carried out with the Murchison Wide-field Array (MWA; Lonsdale et al. 2009; Tingay et al. 2009). GLEAM extends to the entire sky south of declination $+30^\circ$ and is described in detail by Wayth et al. (2009). The survey covers the frequency range between 72 and 231 MHz with the bandwidth of 7.7 MHz. The angular resolution of the survey is $2'.5 \times 2'.2$ ($\delta + 26'.7$) at 154 MHz. The GLEAM data – both the images and the catalogue (Hurley-Walker et al. 2017) – are publicly accessible on the MWA Telescope website.⁶

J0028+0035 is well visible in the map of the TIFR GMRT Sky Survey (TGSS) First Alternative Data Release (ADR1; Intema et al. 2017) conducted at 147.5 MHz. However, the TGSS ADR1 data were compiled without the short-baseline visibilities within 0.2 k λ from the centre of the (u,v)-plane of GMRT. For this reason, extended structures could not be properly imaged and can have underestimated flux densities. Indeed, the flux density of the whole structure of J0028+0035 extracted from the TGSS ADR1 map is 540.5 ± 56.4 mJy. This is much below the flux density measured at similar frequencies with GLEAM and LOFAR – see Table 2. Therefore, we did not use the TGSS ADR1 data in our multifrequency analysis.

We also made use of three large VLA surveys: FIRST, NRAO

⁶ <http://www.mwatelescope.org/gleam>

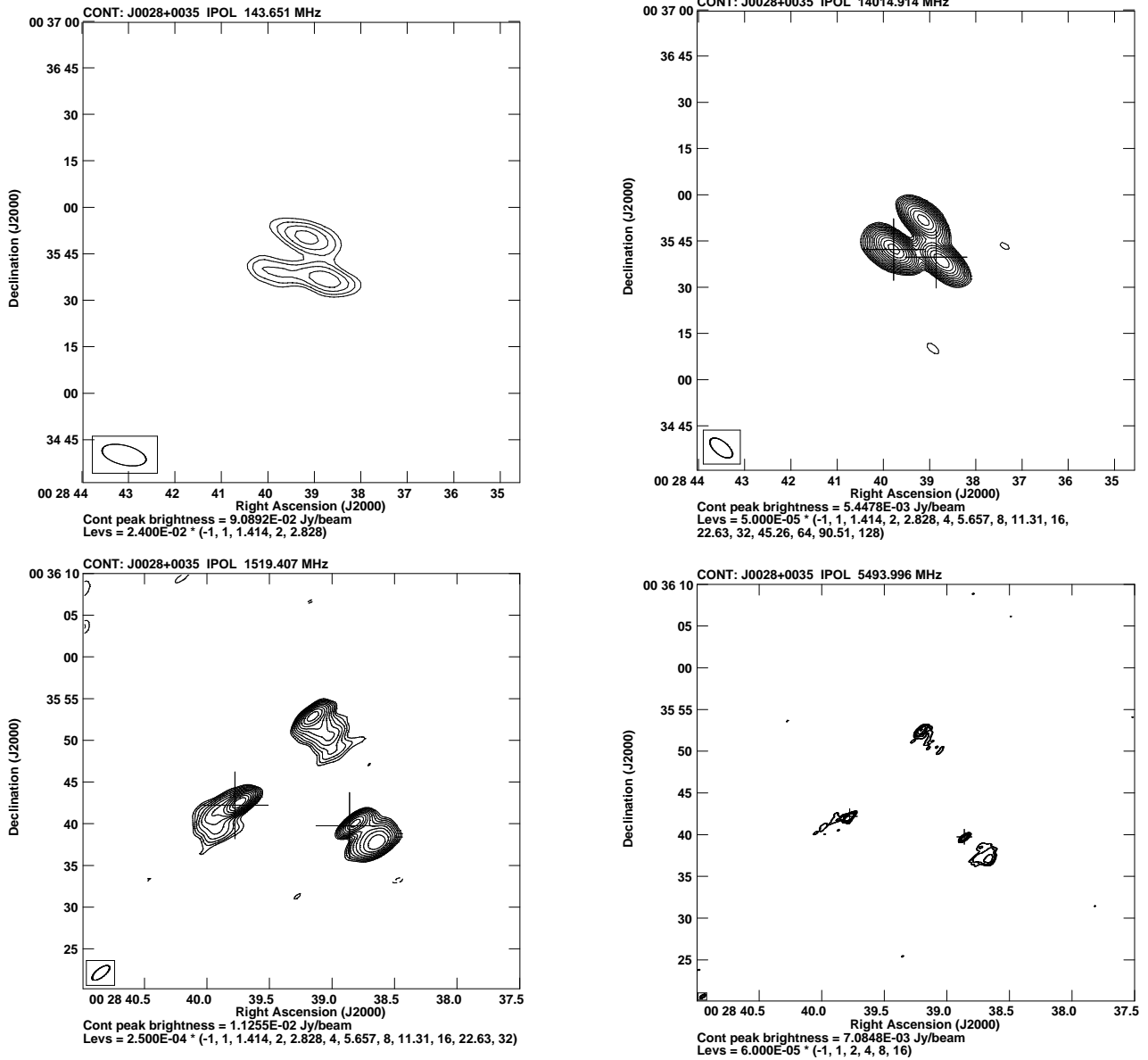


Figure 5. Central part of J0028+0035. Images resulting from LOFAR HBA observations (upper left-hand panel) and the VLA observations at 14015 MHz in D conf. (upper right-hand panel), at 1519 MHz in A conf. (lower left-hand panel), and at 5494 MHz in A conf. (lower right-hand panel). The optical position of the BL Lac object 5BZU J0028+0035 is marked with the left-hand cross. The position of the SDSS J002838.86+003539.7 galaxy is marked with the right-hand cross.

VLA Sky Survey (NVSS; Condon et al. 1998), and VLA Sky Survey (VLASS). At 1400 MHz, we used images extracted from FIRST and NVSS. Since about 60 per cent of the flux density is lost in the high-resolution FIRST maps, the FIRST and NVSS images were combined using `APPS` task `IMERG`. The final merged maps were checked for flux density consistency by comparing the flux density of point sources in the FIRST and merged maps. The differences did not exceed 1 per cent. The 3-GHz data we used come from VLASS, an all-sky (north of declination -40°) survey resulting from observations with the VLA in B-array configuration conducted in a broad bandwidth of 2 – 4 GHz with the angular resolution ~ 2.5 arcsec and final sensitivity of $70 \mu\text{Jy beam}^{-1}$. The VLASS observations began in September 2017 and will finish in 2024. The data of Stokes I, Q, U parameters will be taken in three

epochs to allow for the discovery of variable and transient radio sources. Lacy et al. (2020) presented the science case, the observational strategy for VLASS, and the results from early survey observations. Early results in the form of Quick Look images of Stokes I, which use a relatively simple imaging algorithm that results however in limits on the accuracy, are publicly available.⁷

2.5 Radio morphology of J0028+0035

The VLA A conf. images (Fig. 5, lower panels) unveil the structure of the apparent inner triple. Additionally, we overlaid the

⁷ <https://science.nrao.edu/vlass/vlass-data>

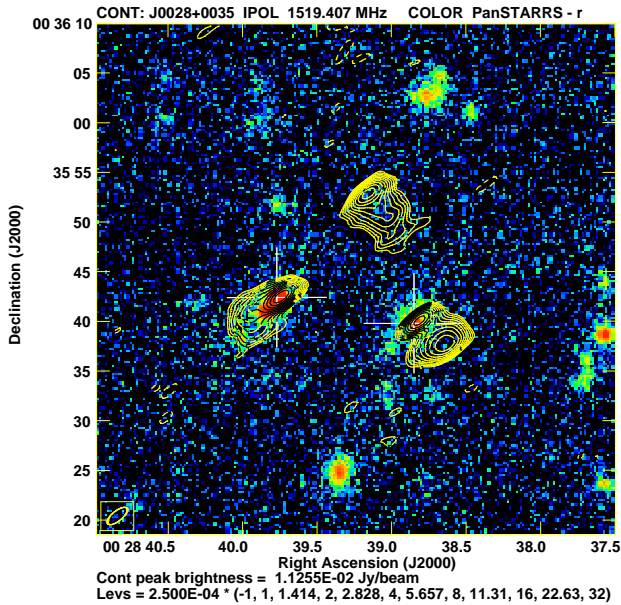


Figure 6. The 1519 MHz VLA A conf. image (contours) overlaid on PanSTARRS *r*-band image.

1519 MHz VLA A conf. image (contours) onto PanSTARRS⁸ *r*-band image (Flewelling et al. 2020) – see Fig. 6. If the eastern component identified with 5BZU J0028+0035 is ignored, the remaining two are clearly an FR II-type mini-double hence J0028+0035 as a whole is, in fact, a DDRS. As seen in these images, 5BZU J0028+0035 is of core-jet type. Given such morphological diversity of those components, the possibility that the inner triple of J0028+0035 is a result of gravitational lensing is unlikely. The feature identified with SDSS J002838.86+003539.7 appears as a separate object in the 5.5 GHz A conf. image (Fig. 5, lower right-hand panel). Although it is located highly asymmetrically between the inner lobes, it might be the core given that such extreme arm-length ratios are encountered in double-lobed radio sources like 3C 254 (Thomasson, Saikia & Muxlow 2006) or 3C 459 (Thomasson, Saikia & Muxlow 2003). It follows that SDSS J002838.86+003539.7 is the host galaxy of J0028+0035. Its spectroscopic redshift extracted from SDSS DR16 (Ahumada et al. 2019) amounts to $z = 0.39846 \pm 0.00008$. It must be noted at this point that the SDSS DR16 spectroscopic redshift of 5BZU J0028+0035 amounts to $z = 0.68632 \pm 0.00025$. The self-evident discrepancy between these two redshifts supports our inference that 5BZU J0028+0035 must be a coincidence.

The host galaxy redshift yields the scale of $5.33 \text{ kpc arcsec}^{-1}$ thus the projected span of the outer lobes is 1093 kpc while that of the inner lobes as measured in the 5.5 GHz VLA A conf. image is 93 kpc . These projected sizes translate to lobe lengths indicated in Table 3 for the assumed jet viewing angle. It follows that J0028+0035 is a giant radio galaxy – see Dabhade et al. (2020), and references therein.

⁸ <https://panstarrs.stsci.edu/>

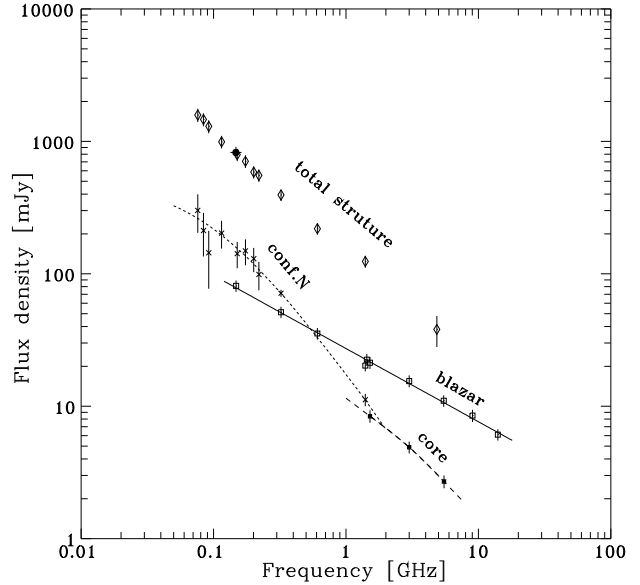


Figure 7. Radio spectrum of the total structure of J0028+0035 and its core, as well as of the confusing source (conf. NE) located near the outer northern lobe and the blazar located in the vicinity of the central structure of J0028+0035

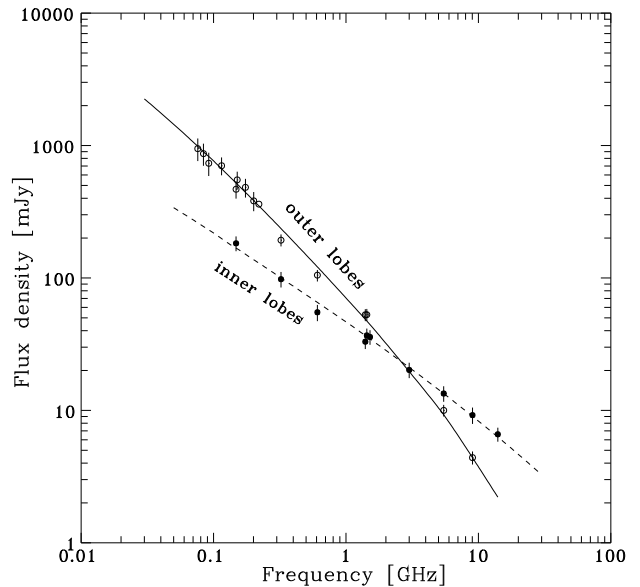


Figure 8. DYNAGE-fitted spectra to the lobes: dashed line – inner lobes, solid line – outer lobes

2.6 Radio spectra of J0028+0035

All the data itemized in Table 2 have been used to construct radio spectra of individual components of the entire observed structure of J0028+0035, i.e. both pairs of its inner and outer lobes, as well as two confusing sources: the blazar in the vicinity of the inner double and the one labelled conf. NE. The latter one cannot be ignored since it is overlain by the MWA GLEAM beam size at the lowest observing frequencies of 76, 84, and 92 MHz. The resulting spectra of the core, the blazar, and conf. NE are confronted in Fig. 7 with the total structure data (column 2 in Table 2).

It shows that the blazar spectrum is described by a pure power-law function (solid line), while the spectrum of the conf. NE source is strongly aged (dotted curve determined with a polynomial function $y = A + Bx + C \exp(\pm x)$).

3 DYNAMICAL EVOLUTION ANALYSIS

3.1 Numerical code

Similarly to Machalski, Jamrozy & Saikia (2009); Machalski, Jamrozy & Konar (2010); Machalski (2011); Marecki, Jamrozy & Machalski (2016), we carried out a dynamical analysis using `DYNAGE` code (Machalski et al. 2007). It is a numerical implementation of an analytical model of the evolution of FR II-type radio source that combines the pure dynamical model of Kaiser & Alexander (1997) and the Kaiser, Dennett-Thorpe & Alexander (1997) (KDA) model of expected radio emission from a source under the influence of the energy loss processes. For a given set of observables, the code allows for solving the inverse problem, i.e. to determine four free parameters of the KDA model (see Table 3): (1) the initial power-law energy distribution of the relativistic electrons p related to the effective injection spectral index α_{inj} , (2) the jet power Q_j , (3) the density of the external gaseous medium near the radio core ρ_0 , and (4) the age of the source's radio structure t . This is obtained by fitting the model to the four observables, including the length and the volume of the lobes, and their radio spectrum, i.e. the slope and normalization at a number of observing frequencies.

3.2 Application of the model and fitting procedure

The analytical model described in Section 3.1 has been applied independently for the inner and outer lobes of J0028+0035. The set of the model parameters with their values assumed for the given pair of lobes is shown in Table 3.

3.2.1 Inner lobes

As a first step, we apply the model to the observational data of the inner lobes because they are determined more precisely than those for the outer ones (columns 4 and 5 vs. columns 8 and 9 of Table 2, respectively). Although the spectra of both inner lobes have been derived, the flux densities of the SW lobe are confused by the radio core at frequencies above 1.5 GHz (column 4 in Table 2). While extraction of the core's spectrum between 1.5 and 5.5 GHz (column 6 in Table 2) has been successful, its extension towards lower frequencies is problematic. An effort made to estimate the core excess in flux densities in column (4) of Table 2, aroused suspicion of a high symmetry in the luminosities of both inner lobes. Unlike in the case of DDRS J1706+4340 (Marecki, Jamrozy & Machalski 2016) where luminosities of the inner lobes are highly asymmetric, the inner lobes of J0028+0035 show unusually asymmetric separation from the core. It is obvious that such asymmetries induce significantly different values of the model parameters for individual lobes. We thus apply the modelling procedure to the whole inner structure setting up its spectrum as a double of the flux densities in column (5) of Table 2 and using one half of the sum of the opposite lobes' lengths.

Following Marecki, Jamrozy & Machalski (2016), we investigate two alternative models. In the first one, a power-law density

distribution of the external gaseous medium with a standard exponent $\beta = 1.5$ is assumed, while in the other one we assume that the inner lobes evolve into an almost uniform medium with $\beta = 0.1$ inside a cocoon formed and inflated by the material of the primary jet flow. We also assume that the lobes are filled with magnetic fields and relativistic particles governed by a relativistic equation of state $\Gamma_l = 4/3$. The best-fitting models results are shown in columns (3) and (4) of Table 5 (predicted flux densities) and in columns (2) and (3) of Table 6 (predicted values of the main model and derivative physical parameters of the inner lobes' structure). The resulting best-fitted spectrum of these lobes – which is almost the same in both models either with $\beta = 1.5$ or with $\beta = 0.1$ – is shown in Fig. 8 (dashed curve).

3.2.2 Outer lobes

As shown in Table 2, the flux densities of the pair of outer lobes are determined at the observing frequency range from 323 MHz up to 9 GHz and supported with the data at the LOFAR HBA frequencies. However, the GLEAM survey data enable supplementing the spectrum of those lobes in the range between 76 and 220 MHz. In order to carry out such a procedure, especially at the lowest frequencies range, we subtract the sum of the inner lobes model fit (column 2 of Table 4; also cf. columns 3 and 4 of Table 5), the blazar extrapolated power-law fit (column 3 of Table 4), and the polynomial-form fit to the GLEAM data (column 4 of Table 4) from the flux densities in column 2 of Table 2.

Likewise to the inner structure, the best-fitting-model-predicted flux densities are shown in column 6 of Table 5 and the model and derivative parameters are shown in column 4 of Table 6. Similarly, the resulting spectrum of the outer lobes is shown in Fig. 8 (solid curve).

4 DISCUSSION

4.1 General remarks

(i) J0028+0035 is one of the most distant DDRSs known – see table 1 in Kuźmicz et al. (2017).

(ii) For frequencies lower than 3 GHz, the total flux density of the outer lobes of J0028+0035 is larger than that of its inner ones. This trend is reversed for frequencies larger than about 3 GHz.

(iii) For comparison with J0028+0035, some characteristic parameters of nine other well-studied DDRSs are presented in Table 7. Noteworthy is the fact that the age of the outer structure of J0028+0035 is one of the largest in this sample, the jet powers for both epochs of activity are similar, and the values of α_{inj} are similar as well. This has already been noticed for DDRSs – see e.g. Konar & Hardcastle (2013).

(iv) J0028+0035 has one of the smallest – 0.085 – inner to outer lobes size ratio among giant DDRSs from Kuźmicz et al. (2017) sample. This is a clear hint that the inner double must be young – see Sect. 4.4.

4.2 Asymmetries of the radio structure of J0028+0035

We already mentioned the asymmetry of the inner structure in Sect. 3.2.1 but this is not the only one in this object. We estimated the bending angle which is the complement of the angle between the lines connecting the brightest points in the lobes with the core. The bending angle is about 11° and 27° for the outer and inner

Table 3. Summary of the model parameters

Parameter (1)	Symbol (2)	Inner lobes (3)	Outer lobes (4)
<i>Observed</i>			
Angular size of lobe ($\times 2$)	LAS	17.4 arcsec	205 arcsec
Length of lobe ($\times 2$)	D	99 kpc	1163 kpc
Aspect ratio of lobe	R_T	3.5	2.6
Radio spectrum; i.e. monochromatic luminosity at a number of observing frequencies; $i = 1, 2, 3, \dots$	α_ν		
	$P_{\nu,i}$	Note(1)	Note(2)
<i>Set</i>			
Adiabatic index of jet material	Γ_j	4/3	4/3
Adiabatic index of lobe material	Γ_ℓ	4/3	5/3
Adiabatic index of ambient medium	Γ_x	5/3	5/3
Adiabatic index of magnetic field	Γ_B	4/3	4/3
Minimum of initial electron Lorentz factor	γ_{\min}	1	1
Maximum of initial electron Lorentz factor	γ_{\max}	10^7	10^7
Core radius of ambient density distribution	a_0	2 kpc	2 kpc
Exponent of ambient density distribution	β	1.5, 0.1	1.5
Jet viewing angle	Θ	70°	70°
<i>Free</i>			
Jet power	$Q_j(W)$		
External density at core radius	$\rho_0(\text{kg m}^{-3})$		
Exponent of initial power-law energy distribution of relativistic electrons	p	$= 1 + 2\alpha_{inj}$	
Source (lobe) age	$t(\text{Myr})$		

(1) and (2) – relevant luminosities are calculated with observed flux densities shown in columns 3 and 5 of Table 5, respectively.

Table 4. Model fit predicted or extrapolated flux densities (in mJy) of different components of the total structure of J0028+0035 used to extract 76–220 MHz flux densities of its outer lobes from the GLEAM data base (shown in column 2 of Table 2)

Frequency MHz (1)	Inner lobes model fit (2)	Blazar lin.extrap. (3)	Conf. NE exp.func.fit. (4)	Sum of column (2)+(3)+(4) (5)	Outer lobes GLEAM data–Sum (6)
76	259.0	113.3	262.3	634.6	947.0
84	242.7	107.2	245.8	595.7	867.9
91.5	229.6	102.2	230.8	562.6	735.0
114.5	198.5	90.3	–	288.8	703.7
150.5	166.0	77.6	–	243.6	550.2
173.5	151.2	71.7	–	222.9	483.7
200.5	137.5	66.2	–	203.7	381.8
219.5	129.5	63.0	–	192.5	361.0

lobes, respectively. We also estimated the arm-length ratio, q , i.e. the ratio of distances between the core and the hotspots or – in the case of the outer lobes that are devoid of hotspots – maxima of radio emission. To find those estimates, we used measurements carried out at 323 MHz (Fig. 3, upper left-hand panel) and at 5494 MHz (Fig. 5, lower right-hand panel). The arm-length-ratio of the outer lobes is $q \approx 1.27$, the southern lobe being the longer whereas the arm-length ratio of the inner lobes is $q \approx 4.33$ and here the northern lobe is the longer one. Such a large asymmetry of the inner lobes of a DDRS is atypical as they are usually more symmetric than the outer ones (Saikia, Konar & Kulkarni 2006; Nandi & Saikia 2012).

According to the standard interpretation, asymmetry of lengths between the two opposite lobes is a light-traveltime effect (see e.g., Longair & Riley 1979). The size ratio between the longer

and shorter lobe amounts to

$$q = [1 + (v_h/c) \cos \theta] / [1 - (v_h/c) \cos \theta],$$

which yields the advance speed of the jets

$$v_h = (q - 1) / (q + 1) (c / \cos \theta).$$

From the values of q determined above along with the condition $|\cos \theta| \leq 1$, we get $v_h/c \geq 0.1189$ and $v_h/c \geq 0.6248$ for the outer and inner lobes, respectively. (Such a dominance of the latter velocity is typical for DDRSs – see e.g. Kaiser et al. (2000); Schoenmakers et al. (2000b); Machalski (2011).) On the other hand, the values of the expansion velocity from the DYNAGE modelling – see Table 6 – are over an order of magnitude smaller. It seems, therefore, that the lobe length asymmetry is not a pure orientation effect. Instead, the inhomogeneity of the intergalactic medium (IGM) may play a role here. Another possibility that

Table 5. Observed (or extracted) flux densities and the best-fitting flux densities (in mJy) for the inner and outer lobes of J0028+0035

Frequency (MHz) (1)	Inner lobes (2)	M $\beta = 1.5$ (3)	odel fit $\beta = 0.1$ (4)	Outer lobes (5)	Model fit (6)
76		259.0 ^a		947±184 ^b	985.7
84		242.7 ^a		868±165 ^b	897.2
91.5		229.6 ^a		735±147 ^b	827.3
114.5		198.5 ^a		704±109 ^b	667.5
147.6	182.5±23	167.8	165.4	468±71	519.3
150.5		166.0 ^a		550±85 ^b	510.7
173.5		151.2 ^a		483±78 ^b	443.6
200.5		137.5 ^a		382±63 ^b	383.7
219.5		129.5 ^a		361±60 ^b	350.2
322.7	97.8±13.1	100.3	99.3	193±20	236.1
607.7	55.0±7.8	65.4	65.3	105±11	121.3
1400.0	33.0±4.0	36.7	37.0	52.7±5.5	48.7
1437.4	36.8±4.6	36.0	36.4	52.8±5.5	47.3
1519.4	35.8±4.5	34.6	35.0		
3000.0	20.2±2.7	21.1	21.4		
5469.1	13.4±1.8	13.4	13.6	10±1	9.3
9016.8	9.2±1.3	9.0	8.9	4.4±0.4	4.4
14014.9	6.6±0.8	6.3	6.1		
χ_{red}^2		0.494	0.572		0.805

^aThe model predicted flux densities shown in column 2 of Table 4.^bThe flux densities extracted from the GLEAM data base (cf. column 6 in Table 4).**Table 6.** Model and derivative parameters for the inner and the outer structure (lobes) of J0028+0035

Parameters (1)	Inner lobes		Outer lobes (4)
	$\beta = 1.5$ (2)	$\beta = 0.1$ (3)	
<i>Model</i>			
α_{inj}	0.63	0.64	0.59
$Q_j(\times 10^{37}\text{W})$	2.17	2.29	2.20
$\rho_0(\times 10^{-22}\text{kg m}^{-3})$	0.081	0.0048	2.67
$t(\text{Myr})$	–	–	245
$t_j(\text{Myr})$	3.2	3.6	234
<i>Derivative</i>			
$v_h/c(\times 10^{-3})$	43.2	27.4	6.77
$\rho_{(D/2)}(\times 10^{-24}\text{kg m}^{-3})$	0.066	0.3475	0.054
$p_t(\times 10^{-13}\text{N m}^{-2})$	7.60	6.78	0.26
$B_t(\text{nT})$	1.61	1.52	0.28

could also be taken into account is that the changes of the bending angle of the external and internal structure may indicate that the jet changes its orientation between the two epochs of activity. A change of the direction of the inner and outer structures' jets is not exceptional in DDRSs. In Section 1, we already mentioned J2333–2343 but also the morphologies of J1352+3126 (3C 293; Bridle, Fomalont & Cornwell 1981; Akujor et al. 1996; Beswick et al. 2004; Joshi et al. 2011; Machalski et al. 2016), J0709–3601 (Subrahmanyan, Saripalli & Hunstead 1996; Saripalli et al. 2013), and J1328+2752 (Nandi et al. 2017) show clear evidence for the restart of the jets' activity accompanied by their substantial axis change. Moreover, GRGS J0009+1244 (4C 12.03; Leahy & Perley 1991) and GRGS J1513+2607 (3C 315;

Saripalli & Subrahmanyan 2009) have large-scale X-shaped morphologies which may also be caused by that.

4.3 Density, pressure, and kinetic temperature

J0028+0035 lacks X-ray observations, which makes direct estimation of the parameters of the IGM surrounding this DDRS – i.e. density, pressure, and kinetic temperature – impossible. Nevertheless, crude estimates of the ambient kinetic temperature and the sound speed in the ambient gaseous environment are possible using the physical parameters shown in Table 6. From the equation of state for a perfect gas, $p = nkT$, one can find that

$$kT = \mu m_{\text{H}} p / \rho \sim \mu m_{\text{H}} p_l / \rho_{(D/2)},$$

where $n = \rho / \mu m_{\text{H}}$ and p_l is the pressure inside the lobe. The value of the ambient density at the end of the lobe, $\rho_{(D/2)}$, along with other necessary parameters' values are shown in Table 6. Assuming the mean molecular weight for ionized gas $\mu = 0.62$, we find for the outer lobes $kT = 3.1$ keV. It follows that the sound speed $c_s = [(\Gamma_x kT) / (\mu m_{\text{H}})]$ for the outer lobes amounts to $0.00298 c$ and the ratio $v_h / c_s = 2.27$. This means that the longitudinal expansion of these lobes is still supersonic. Although no hotspots can be seen in the outer lobes, traces of bow shocks are visible in the low-frequency radio maps – see the upper panel of Fig. 3. The compatibility of the above ambient temperature with the X-ray temperatures in samples of powerful radio sources (Belsole et al. 2007) is worth noting.

To estimate the kinetic temperature inside the cocoon surrounding the inner lobes, whose gaseous environment is likely to be modified by the jet flow during the earlier phase of activity, we apply the model of $\beta = 0.1$ that corresponds to a rather smooth medium. We find $kT = 12.6$ keV and $c_s = 0.00612 c$. Dividing the

Table 7. Properties of J0028+0035 and selected DDRSs

Source J2000 name (1)	z (2)	$\log M_{\text{BH}}^c$ (M_{\odot}) (3)	l_{inn}^c (kpc) (4)	l_{out}^c (kpc) (5)	$\alpha_{\text{inj}}^{\text{inn}}$ (6)	$\alpha_{\text{inj}}^{\text{out}}$ (7)	t_{in} (Myr) (8)	t_{out} (Myr) (9)	t_{quies} (Myr) (10)	$Q_{\text{j}}^{\text{inn}}$ ($\times 10^{37}$ W) (11)	$Q_{\text{j}}^{\text{out}}$ ($\times 10^{37}$ W) (12)	Reference (13)
J0028+0035	0.3985	8.16	93	1093	0.64	0.59	3.6	245	11	2.29	2.20	p
J0041+3224	0.45 ^b	–	172	974	0.60	0.62	4.0	105	11	2.49	14.4	1
J0116–4722 ^a	0.1461	–	445	1441	0.70	0.62	1.00–28.00	66–236	1.4–65.4	–	–	2, 7
J0840+2949 ^a	0.0647	8.32	39	533	0.83	0.81	0.12–33.00	> 200	2.0–102.0	–	–	3, 7
J1158+2621 ^a	0.1121	7.96	139	484	0.77	0.79	0.50–4.90	113	6.6–11.0	–	1.7	2, 7
J1352+3126	0.045	8.15	1	180	0.59	0.61	0.3	62	0.7	0.21	0.21	4
J1453+3308	0.2482	9.02	159	1299	0.66	0.50	5.0	104	24	0.32	3.92	1
J1548–3216	0.1082	–	312	962	0.61	0.51	9.2	132	30	0.14	1.59	1
J1706+4340	0.525 ^b	–	194	687	0.55	0.53	12	260–300	27	2.63	2.59	5
J1835+6204 ^a	0.5194	–	372	1378	0.86	0.82	1.34–2.25	22	1.0–6.6	–	28.5	6, 7

References – p: this paper, 1: Machalski et al. (2011), 2: Konar et al. (2013), 3: Jamroz et al. (2007), 4: Machalski et al. (2016), 5:

Marecki, Jamroz & Machalski (2016), 6: Konar et al. (2012), 7: Konar & Hardcastle (2013). Column description is as follows: Column 1: J2000 name of the source, Column 2: redshift of the source, Column 3: black hole mass, Columns 4 and 5: size of the inner and outer double, respectively, Columns 6 and 7: alpha injection of the inner and outer double, respectively, Columns 8 and 9: age of the inner and outer double, respectively, Column 10: duration of the quiescent phase, Columns 11 and 12: jet power of the inner and outer double, respectively, Column 13: reference to the spectral age and other parameters of the source. ^aFor this source the data have been taken from spectral modelling rather than from dynamical modelling as for other sources. ^bPhotometric redshift. ^cData taken from or calculated according to Kuźmicz et al. (2017).

corresponding values of the advance speed of the inner lobes v_{h} (see Table 6) by the relevant sound speed obtained above, we find the Mach number of 4.56. This value is twice as large as that for the outer lobes and the obtained kinetic temperature is four times higher. Meanwhile, the overall temperature of the very luminous cluster of galaxies RX J1347.5–1145 is $kT \sim 10$ keV (Allen et al. 2002; Gitti et al. 2004). The high value of kT of the inner lobes of J0028+0035 is, however, comparable to the one Birzan et al. (2017) found for some high-redshift AGNs. Although the model with $\beta = 1.5$ has a lower value of χ_{red}^2 (see the last row of Table 5), it leads to a prohibitively high value of kinetic temperature for the inner lobes thus it has to be rejected.

4.4 Age and intermittent activity

The age solutions for the inner and outer lobes collected in Table 6 suggest that the last renewal of the jet activity took place about 3.6 Myr ago hence its present age is about 1.3 per cent of the age estimated for the outer lobes' structure. On the other hand, the length of the period of quiescence emerging from the model fits, $t - t_{\text{j}}$, is of about 11 Myr. These values, when compared with those for other DDRSs listed in Table 7, appear as typical. However, the ratio of inner to outer lobes' age for J0028+0035 is one of the lowest among those objects. (The only clear exception is J1352+3126.)

Assuming similar dynamical and spectral age of the inner structure and taking into account the dynamically estimated age of 3.6 Myr, and magnetic field strengths of 1.52 nT we calculated the break frequency of the synchrotron emission to be of about 32 GHz. It would be possible to prove the above estimation with sensitive VLA observations at K band (18 – 26.5 GHz), Ka band (26.5–40 GHz) and Q band (40–50 GHz) and/or, in the future, with the Atacama Large Millimeter/submillimeter Array using band 1 (35 – 50 GHz) receiver.

5 SUMMARY

(i) We conducted an observing campaign targeted at J0028+0035, a giant radio source that has atypical morphology: a triple straddled by a pair of relic lobes (Fig. 1). It was observed with LOFAR, GMRT, and the VLA at a variety of frequencies (Table 1). We present the images resulting from those observations (Figs 2–5). The conclusion we draw from that observational material is that the inner triple consists of an FR II-type double pertinent to J0028+0035 and a coincident source 5BZU J0028+0035 – a BL Lac object whose redshift ($z = 0.68632$) does not correspond with that of the host galaxy of J0028+0035 ($z = 0.39846$). Therefore, J0028+0035 as a whole is a double–double source.

(ii) We supplemented the flux density measurements made using our data with those extracted from a number of radio sky surveys (Table 2). With that data base covering a very wide frequency range from 74 MHz to 14 GHz, we constructed the radio spectra (Fig. 7) of different parts of J0028+0035. We modelled those spectra with DYNAGE code (Fig. 8). This way we were able to determine physical parameters for both the outer and the inner lobes (Table 6).

(iii) We compared the values of some of those parameters derived for J0028+0035 with the values of respective parameters for a number of DDRS (Table 7). It appears that J0028+0035 is a well-behaved DDRS. In particular, it has a property of many DDRSs: for a given object its $\alpha_{\text{inj}}^{\text{inn}}$ and $\alpha_{\text{inj}}^{\text{out}}$ are similar. Similarity of $Q_{\text{j}}^{\text{inn}}$ and $Q_{\text{j}}^{\text{out}}$ is also striking. These circumstances are in line with our conclusion that J0028+0035 is a *bona fide* DDRS which was so far not recognized as such only because of the eastern component of the inner triple being a coincidence.

(iv) We found the age of the outer and the inner lobes of J0028+0035 – 245 and 3.6 Myr, respectively – and the length of quiescence between the two active phases – 11 Myr.

(v) We argue that the inner lobes evolve into an almost uniform medium inside a cocoon surrounding them. Since it has been modified by the jet flow during the previous active phase of AGN, the power-law density distribution of the gaseous medium with a stan-

ard exponent $\beta = 1.5$ cannot be adopted here. Otherwise, the obtained values of kinetic temperatures become unrealistic.

ACKNOWLEDGEMENTS

This work is (partly) based on data obtained with the ILT. LOFAR (van Haarlem et al. 2013) is the Low Frequency Array designed and constructed by ASTRON. It has observing, data processing, and data storage facilities in several countries, that are owned by various parties (each with their own funding sources), and that are collectively operated by the ILT foundation under a joint scientific policy. The ILT resources have benefited from the following recent major funding sources: CNRS-INSU, Observatoire de Paris and Université d'Orléans, France; BMBF, MIWF-NRW, MPG, Germany; Science Foundation Ireland (SFI), Department of Business, Enterprise and Innovation (DBEI), Ireland; NWO, The Netherlands; The Science and Technology Facilities Council, UK; Ministry of Science and Higher Education (MSHE), Poland. We thank the MSHE for granting funds for the Polish contribution to the ILT (MSHE decision no. DIR/WK/2016/2017/05-1) and for maintenance of the LOFAR PL-610 Borowiec, LOFAR PL-611 Łazy, and LOFAR PL-612 Baldy stations. These data were (partly) processed by the LOFAR Two-Metre Sky Survey (LoTSS) team. This team made use of the LOFAR direction-independent calibration pipeline (<https://github.com/lofar-astron/prefactor>), which was deployed by the LOFAR e-infragroup on the Dutch National Grid infrastructure with support of the SURF Co-operative through grants e-infra 160022 and e-infra 160152 (Mechev et al. 2017). The LoTSS direction-dependent calibration and imaging pipeline (<http://github.com/mhardcastle/ddf-pipeline/>) was run on compute clusters at Leiden Observatory and the University of Hertfordshire, which are supported by a European Research Council Advanced Grant [NEWCLUSTERS-321271] and the UK Science and Technology Funding Council [ST/P000096/1].

We thank the staff of GMRT that made these observations possible. GMRT is run by the National Centre for Radio Astrophysics of the Tata Institute of Fundamental Research.

The National Radio Astronomy Observatory running the VLA is a facility of the National Science Foundation operated under cooperative agreement by Associated Universities, Inc.

Funding for the Sloan Digital Sky Survey IV has been provided by the Alfred P. Sloan Foundation, the U.S. Department of Energy Office of Science, and the Participating Institutions. SDSS-IV acknowledges support and resources from the Center for High-Performance Computing at the University of Utah. The SDSS web site is www.sdss.org. SDSS-IV is managed by the Astrophysical Research Consortium for the Participating Institutions of the SDSS Collaboration including the Brazilian Participation Group, the Carnegie Institution for Science, Carnegie Mellon University, the Chilean Participation Group, the French Participation Group, Harvard-Smithsonian Center for Astrophysics, Instituto de Astrofísica de Canarias, The Johns Hopkins University, Kavli Institute for the Physics and Mathematics of the Universe (IPMU) / University of Tokyo, the Korean Participation Group, Lawrence Berkeley National Laboratory, Leibniz Institut für Astrophysik Potsdam (AIP), Max-Planck-Institut für Astronomie (MPIA Heidelberg), Max-Planck-Institut für Astrophysik (MPA Garching), Max-Planck-Institut für Extraterrestrische Physik (MPE), National Astronomical Observatories of China, New Mexico State University, New York University, University of Notre Dame, Observatório Nacional / MCTI, The Ohio State University, Pennsylvania State

University, Shanghai Astronomical Observatory, United Kingdom Participation Group, Universidad Nacional Autónoma de México, University of Arizona, University of Colorado Boulder, University of Oxford, University of Portsmouth, University of Utah, University of Virginia, University of Washington, University of Wisconsin, Vanderbilt University, and Yale University.

The Pan-STARRS1 Surveys (PS1) and the PS1 public science archive have been made possible through contributions by the Institute for Astronomy, the University of Hawaii, the Pan-STARRS Project Office, the Max-Planck Society and its participating institutes, the Max Planck Institute for Astronomy, Heidelberg and the Max Planck Institute for Extraterrestrial Physics, Garching, The Johns Hopkins University, Durham University, the University of Edinburgh, the Queen's University Belfast, the Harvard-Smithsonian Center for Astrophysics, the Las Cumbres Observatory Global Telescope Network Incorporated, the National Central University of Taiwan, the Space Telescope Science Institute, the National Aeronautics and Space Administration under Grant No. NNX08AR22G issued through the Planetary Science Division of the NASA Science Mission Directorate, the National Science Foundation Grant No. AST-1238877, the University of Maryland, Eötvös Loránd University (ELTE), the Los Alamos National Laboratory, and the Gordon and Betty Moore Foundation.

MJ and JM were supported by Polish National Science Centre grant UMO-2018/29/B/ST9/01793.

We are grateful to the referee for a large number of useful suggestions.

DATA AVAILABILITY

The data underlying this paper will be shared on reasonable request to the corresponding author.

REFERENCES

- Ahumada R., et al., 2020, *ApJS*, 249, 3
 Akujor C. E., Leahy J. P., Garrington S. T., Sanghera H., Spencer R. E., Schilizzi R. T., 1996, *MNRAS*, 278, 1
 Allen S. W., Schmidt R. W., Fabian A. C., 2002, *MNRAS*, 335, 256
 Baars J. W. M., Genzel R., Pauliny-Toth I. I. K., Witzel A., 1977, *A&A*, 61, 99
 Bagchi J., Vivek M., Vikram V., Hota A., Biju K. G., Sirothia S. K., Srianand R., Gopal-Krishna, Jacob J., 2014, *ApJ*, 788, 174
 Becker R. H., White R. L., Helfand D. J., 1995, *ApJ*, 450, 559
 Belsole E., Worrall D. M., Harcastle M. J., 2007, *MNRAS*, 381, 1109
 Beswick R. J., Peck A. B., Taylor G. B., Giovannini G., 2004, *MNRAS*, 352, 49
 Birzan L., Rafferty D. A., Bruggen M., Intema H. T., 2017, *MNRAS*, 471, 1766
 Bridle A. H., Fomalont E. B., Cornwell T. J., 1981, *AJ*, 86, 1294
 Brocksopp C., Kaiser C. R., Schoenmakers A. P., de Bruyn A. G., 2007, *MNRAS*, 382, 1019
 Cohen, A. S., Lane, W. M., Cotton, W. D., Kassim, N. E., Lazio, T. J. W., Perley, R. A., Condon, J. J., Erickson, W. C., 2007, *AJ*, 134, 2245
 Condon J. J., Cotton W. D., Greisen E. W., Yin Q. F., Perley R. A., Taylor G. B., Broderick J. J., 1998, *AJ*, 115, 1693
 Dabhade P. et al., 2020, *A&A*, 642, A153

- Flewelling H. A. et al., 2020, *ApJS*, 251, 7
- Gitti M., Schindler S., 2004, *A&A*, 427, L9
- Gregory P. C., Condon J. J., 1991, *ApJS*, 75, 1011 (87GB)
- Hernandez-Garcia L. et al., 2017, *A&A*, 603, 131
- Hota A., Sirothia S. K., Ohya Y., Konar C., Kim S., Rey S.-C., Saikia D. J., Croston J. H., Matsushita S., 2011, *MNRAS*, 417L, 36
- Hurley-Walker N. et al., 2017, *MNRAS*, 464, 1146
- Intema H. T., 2009, Ph.D. Thesis, Leiden University
- Intema H. T., 2014, SPAM, Astrophysics Source Code Library, ascl:1408.006
- Intema H. T., van der Tol S., Cotton W. D., Cohen A. S., van Bemmell I. M., Röttgering H. J. A., 2009, *A&A*, 501, 1185
- Intema H. T., Jagannathan P., Mooley K. P., Frail D. A., 2017, *A&A*, 598, 78
- Ishwara-Chandra C. H., Taylor A. R., Green D. A., Stil J. M., Vaccari M., Ocran E. F., 2020, *MNRAS*, 497, 5383
- Jamrozy M., Konar C., Saikia D.J., Stawarz Ł., Mack K.-H., Siemiginowska A., 2007, *MNRAS*, 378, 581
- Jamrozy M., Saikia D. J., Konar C., 2009, *MNRAS*, 399L, 141
- Joshi S. A., Nandi S., Saikia D. J., Ishwara-Chandra C. H., Konar C., 2011, *MNRAS*, 414, 1397
- Kaiser C. R., Alexander P., 1997, *MNRAS*, 286, 215
- Kaiser C. R., Dennett-Thorpe J., Alexander P., 1997, *MNRAS*, 292, 723
- Kaiser C. R., Schoenmakers A. P., Röttgering H. J. A., 2000, *MNRAS*, 315, 381
- Komissarov S. S., Gubanov A. G., 1994, *A&A*, 285, 27
- Konar C., Hardcastle M.J., Jamrozy M., Croston J.H., Nandi S., 2012, *MNRAS*, 424, 1061
- Konar C., Hardcastle M.J., Jamrozy M., Croston J.H., 2013, *MNRAS*, 430, 2137
- Konar C., Hardcastle M.J., 2013, *MNRAS*, 436, 1595
- Konar C., Saikia D. J., Jamrozy M., Machalski J., 2006, *MNRAS*, 372, 693
- Kuźnicz A., Jamrozy M., Kozieł-Wierzbowska D., Weźgowiec M., 2017, *MNRAS*, 471, 3806
- Lacy M., Baum S. A., Chandler C. J., 2020, *PASP*, 132, 035001
- Lane W. M., Cotton W. D., Helmboldt J. F., Kassim N. E., 2012, *RaSc*, 47, RS0K04
- Lane W. M., Cotton W. D., van Velzen S., Clarke T. E., Kassim N. E., Helmboldt J. F., Lazio T. J. W., Cohen A. S., 2014, *MNRAS*, 440, 327
- Leahy J. P., Perley R. A., 1991, *AJ*, 102, 537
- Longair M. S., & Riley J. M., 1979, *MNRAS*, 188, 625
- Lonsdale C. J. et al., 2009, *IEEEP*, 97, 1497
- Machalski J., Chyży K. T., Stawarz Ł., Kozieł D., 2007, *A&A*, 462, 43
- Machalski J., Jamrozy M., Saikia D. J., 2009, *MNRAS*, 395, 812
- Machalski J., Jamrozy M., Konar C., 2010, *A&A*, 510, A84
- Machalski J., 2011, *MNRAS*, 413, 2429
- Machalski J., Jamrozy M., Stawarz Ł., Kozieł-Wierzbowska D., 2011, *ApJ*, 740, 58
- Machalski J., Jamrozy M., Stawarz Ł., Weźgowiec M., 2016, *A&A*, 595, A46
- Mahatma V. H. et al. 2019, *A&A*, 622, A13
- Marecki A., Jamrozy M., Machalski J., 2016, *MNRAS*, 463, 338
- Massaro E., Giommi P., Leto C., Marchegiani P., Maselli A., Perri M., Piranomonte S., Sclavi S., 2009, *A&A*, 495, 691
- Mechev A., Oonk J. B. R., Danezi A., Shimwell T. W., Schrijvers C., Intema H., Plaata A., Röttgering H. J. A., 2017, Proceedings of the International Symposium on Grids and Clouds (ISGC) 2017, PoS(ISGC2017)002 (<https://pos.sissa.it/293/002>)
- Nandi S., Saikia D. J., 2012, *BASI*, 40, 121
- Nandi S., Jamrozy M., Roy R., Larsson J., Saikia D. J., Baes, M., Singh M., 2017, *MNRAS*, 467L, 56
- Nandi S. et al., 2019, *MNRAS*, 486, 5158
- Pajdosz-Śmierciak U., Jamrozy M., Soida M., Stawarz Ł., 2018, *ApJ*, 868, 64
- Proctor D. D., 2011, *ApJS*, 194, 31
- Roger R. S., Bridle A. H., Costain C. H., 1973, *AJ*, 78, 1030
- Saikia D. J., Jamrozy M., 2009, *BASI*, 37, 63
- Saikia D. J., Konar C., Kulkarni V. K., 2006, *MNRAS*, 366, 1391
- Saripalli L., Malarecki J. M., Subrahmanyam R., Jones D. H., Staveley-Smith L., 2013, *MNRAS*, 436, 690
- Saripalli L., Subrahmanyam R., 2009, *ApJ*, 695, 156
- Schoenmakers A. P., de Bruyn A. G., Röttgering H. J. A., van der Laan H., Kaiser C. R., 2000a, *MNRAS*, 315, 371
- Schoenmakers A. P., de Bruyn A. G., Röttgering H. J. A., van der Laan H., 2000b, *MNRAS*, 315, 395
- Shimwell T. W. et al., 2017, *A&A*, 598, A104
- Siemiginowska A., Stanghellini C., Brunetti G., Fiore F., Aldcroft T. L., Bechtold J., Elvis M., Murray S. S., Antonelli L. A., Colafrancesco S., 2003, *ApJ*, 595, 643
- Singh V., Ishwara-Chandra C. H., Kharb P., Srivastava S., Janardhan P., 2016, *ApJ*, 826, 132S
- Spergel D. N. et al., 2003, *ApJS*, 148, 175
- Subrahmanyam R., Saripalli L., Hunstead R. W., 1996, *MNRAS*, 279, 257
- Swarup G., Ananthakrishnan S., Kapahi V.K., Rao A.P., Subrahmanya C.R., Kulkarni V.K., 1991, *Curr. Sci.*, 60, 95
- Thomasson P., Saikia D. J., Muxlow T. W. B., 2003, *MNRAS*, 341, 91
- Thomasson P., Saikia D. J., Muxlow T. W. B., 2006, *MNRAS*, 372, 1607
- Tingay S. J. et al., 2013, *PASA*, 30, 7
- Wayth R. B. et al. 2015, *PASA*, 32, 25
- van Haarlem M. P. et al., 2013, *A&A*, 556, A2
- van Weeren R. J., Williams W. L., Hardcastle M. J., 2016, *ApJSS*, 223, 1